Braz J Phys (2015) 45:525–531
DOI 10.1007/s13538-015-0344-9

SOCIEDADE BRASILEIRA DE FÍSICA

CONDENSED MATTER

Effective Thermal Diffusivity Study of Powder Biocomposites via Photoacoustic Method

V. V. G. Mariucci[1] · J. A. da Cruz[1] · T. G. M. Bonadio[1] · A. M. Picolloto[1] · W. R. Weinand[1] · W. M. Lima[1] · A. N. Medina[1] · A. C. Bento[1]

Received: 16 March 2015 / Published online: 21 July 2015

Abstract The effective thermal diffusivity for biocomposites of hydroxyapatite (HAp), and niobium pentoxide (Nb_2O_5) on powder form was studied via photoacoustic method adapted for porous materials. The concentration of each element was accompanied with the results of X-ray diffractometer (XRD) and scanning electron microscopy (SEM). A theoretical model for the thermal coupling of a three layered sample, designed to contain the powder material is proposed. The method for mixtures obeyed the formula $[(1-x)HAp + (x)Nb_2O_5]$ for $0.0 \leq x \leq 1.0$. Experimental results for effective thermal diffusivity ranged between $(6.4 \pm 0.3) \times 10^{-6}$ m^2 s^{-1} and $(9.8 \pm 0.4) \times 10^{-6}$ m^2 s^{-1} for $x \leq 0.7$. Values of the effective thermal diffusivity have decreased sharply to $(0.70 \pm 0.03) \times 10^{-6}$ m^2 s^{-1} for $x > 0.7$. SEM micrographs showed a coating of HAp over the particles of Nb_2O_5 for some mixtures.

Keywords Biocompatible material · Effective thermal diffusivity · Photoacoustic · Powder metallurgy

1 Introduction

Hydroxyapatite (HAp) is widely studied in its natural state, or as coating, obtained by techniques like the plasma spray process (i.e., when necessary to obtain a very thin layer onto a metallic substrate like (Ti), (Pt), or some metallic alloys) [1, 2]. Recently, another material draws attention in several studies, the niobium pentoxide Nb_2O_5, is employed to compose many technological objects like humidity sensors and thin films for electronic components (capacitors, electrochromic devices, and catalytic surfaces) [3]. Developing new materials to replace damaged bones or body parts that do not work properly has encouraged some important studies in various areas of research [4–6]. Calcium phosphate, one of it, when crystallized as hydroxyapatite $[Ca_{10}(PO_4)_6(OH)_2]$ contains properties such as biocompatibility and bioactivity [7]. The relative amount of calcium and phosphorus in the HAp is approximately equal to the amount measured in natural bone and teeth. Ratio of calcium and phosphorus is given by $[10Ca]/[6P] \approx 1.67$, that makes the HAp a positive choice for restoration of bone or cartilage parts in humans [5, 8]. The mechanical fragility, however, may be one disadvantage of HAp compared to natural bone. By mixing other materials, it is possible to improve some properties: decrease the density and increase both the mechanical strength and corrosion resistance. There might also be a decrease related to toxicity, and an improvement in the correct conformation regarding the mechanical function in the body. Powder metallurgy techniques favors the obtention of composites for various applications. The niobium (Nb), or niobium pentoxide Nb_2O_5 are materials that can be mixed with HAp to obtain composites with mechanical properties similar to natural bone. Also, niobium and several of its derivatives are abundant in Brazil, making them low-cost materials for studies and for use in many technological areas [9].

Some previous studies on biocompatible materials, especially on nanostructured composites with different percent concentrations of niobium pentoxide [8, 10–12], were con-

✉ V. V. G. Mariucci
vgmariucci@hotmail.com; pg51508@uem.br

[1] Departamento de Física, Universidade Estadual de Maringá, Av. Colombo 5790, Maringá-PR, 87020-900, Brazil

tinued in this research with these types of mixtures. A photoacoustic technique, however, was used on determining the effective thermal diffusivity of the precursors before any transformation process as sintering, pressing, or chemical reactions. To better compare the proportions of each element and its thermal effects along the powder mixtures, diffraction measurements of X-rays (XRD) and scanning electron microscopy (SEM) were performed.

Thermal characterization of porous media arouses interest in many technological applications, for instance: in the powder metallurgy, pharmacy, thermal insulation, and soil characterization. Usually, the analysis of heat diffusion in a porous media becomes difficult due to its complicated structures. Since the thermal properties of solid and fluid phases are different, the way the solid is interconnected can affect substantially the heat conduction [13]. Several experimental and theoretical approaches have been developed to describe the propagation of heat in porous materials, each of them with their limitations [13–15].

2 Theory

2.1 Heat Transfer Model

A theoretical model similar to that developed by Balderas-López and Mandelis [16, 17] used on determining the thermal diffusivity for multilayered systems or liquids was applied. The difference between the model of Balderas-López and Mandelis and the theoretical model proposed in this work lies on the sample's configuration: a porous medium enclosed by two metallic layers. The model considers only the thermal diffusion process, and discard the contributions by convective or irradiation effects for generation of photoacoustic signal. Such effects were assumed to be very low within the powder. Figure 1 shows the geometry of the model. Layer 1 conducts the heat generated by modulated light to the sample, and layer 2 conducts the heat that emanate from the sample to the gas chamber coupled with microphone. The heat diffusion on each layer is governed by Eq. 1.

$$\frac{\partial^2 T_i}{\partial x^2} + \frac{1}{\alpha_i} \cdot \frac{\partial T_i}{\partial t} = S_i \tag{1}$$

α_i is thermal diffusivity in units of ($m^2\ s^{-1}$), S_i is the heat source term, and sub-index i denotes each layer (ex = external gas, 1 = layer 1, s = powder sample, 2 = layer 2, and g = gas chamber). The thermal coupling for all equations is given by the one-dimensional limits shown in Fig. 1. Layer 1 has a heat source $S_1 = (\beta' Q_0/2k_1)(1+e^{j\omega t})$, being β' a constant with dimensions given by ($WJ^{-1}\ m^{-3}$), Q_0 the total heat in Joules (J) transferred in the optical absorption [18], and k_1 ($W(mK)^{-1}$) the thermal conductivity of the material. For other layers is assumed the heat source as null. The solution to Eq. 1 for layer 1 is given by Eq. 2, while for other layers, solutions are given by Eq. 3:

$$T_1(x,t) = \overbrace{u_1 + v_1 x + \lambda_1 x^2}^{\text{Timeless term}} + \overbrace{\left(A_1 e^{\sigma_1 x} + B_1 e^{-\sigma_1 x} - \frac{2\lambda_1}{\sigma_1^2}\right) e^{j\omega t}}^{\text{Time dependent term}} \tag{2}$$

$$T_i(x,t) = u_i + v_i x + (A_i e^{\sigma_i x} + B_i e^{-\sigma_i x}) e^{j\omega t} \tag{3}$$

u_i and v_i are time independent contributions for temperature variation, $\sigma_i = (1+j)a_i$, $a_i = (\pi f/\alpha_i)^{1/2}$, $\lambda_1 = (Q_0\beta'/4k_1)$, f is the optical modulation frequency and $j = \sqrt{-1}$ is the imaginary unit. Once the photoacoustic signal is generated by periodic light incidence, the temperature fluctuation in gas chamber is determined by the temporal term in Eq. 3 (designated by $T_g(x,t)$). Assuming $\lim_{x\to -(l_g+l_2)} T_g(x,t) = T_0$ is valid for any time (T_0 is the room temperature), and solving for B_g, we get $B_g = T_0 e^{-a_g(l_g+l_2)} e^{-j(l_g+l_2)a_g}$. Analyzing the last expression for B_g one conclude, for $f = 0$ $B_g = T_0$ and is time independent. As frequency is increased, $|B_g| \to 0$. So, it is possible to do an approximation for temperature variation near the sample surface ($x = -l_2$) due to only A_g, which is given by Eq. 4.

$$A_g = -\frac{\eta}{\sigma_1^2 \chi_T} \tag{4}$$

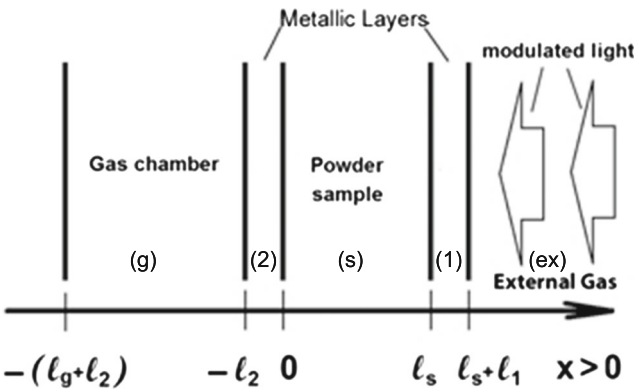

Fig. 1 Geometry for heat propagation used on the proposed photoacoustic model

with η and χ_T as follows:

$$\begin{aligned}
\eta &= 2e^{(-l_1\sigma_1+2l_s\sigma_1+l_s\sigma_g)}(e^{l_1\sigma_1}-1)\\
&\quad\times[1-\epsilon_2+e^{l_1\sigma_1}(1+\epsilon_2)]\epsilon_s\lambda_1\\
\chi_T &= \chi_1\cdot\chi_2+\chi_3\cdot\chi_4\\
\chi_1 &= -e^{l_s\sigma_1}[(\epsilon_2\epsilon_s-1)\cosh(l_1\sigma_1)\\
&\quad+(\epsilon_s-\epsilon_2)\mathrm{senh}(l_1\sigma_1)]\\
\chi_2 &= e^{l_s\sigma_1}[(\epsilon_2\epsilon_s-1)\cosh(l_2\sigma_2)\\
&\quad+(\epsilon_s-\epsilon_2)\mathrm{senh}(l_2\sigma_2)]\\
\chi_3 &= e^{l_s(\sigma_1+\sigma_s)}[(\epsilon_2\epsilon_s+1)\cosh(l_1\sigma_1)\\
&\quad+(\epsilon_s+\epsilon_2)\mathrm{senh}(l_1\sigma_1)]\\
\chi_4 &= e^{l_s(\sigma_1+\sigma_s)}[(\epsilon_2\epsilon_s+1)\cosh(l_2\sigma_2)\\
&\quad+(\epsilon_s+\epsilon_2)\mathrm{senh}(l_2\sigma_2)]
\end{aligned}$$

with $\epsilon_s = \frac{k_2}{k_s}\sqrt{\frac{\alpha_s}{\alpha_2}}$ and $\epsilon_2 = \frac{k_g}{k_1}\sqrt{\frac{\alpha_1}{\alpha_g}}$. Therefore, it follows that $T_g(x,t) = A_g e^{\sigma_g x+j\omega t}$. As proposed by Rosencwaig and Gersho [19, 20], the amplitude of the pressure fluctuation inside the microphone's acoustic cavity can be expressed by:

$$\langle P\rangle = \frac{\gamma P_0}{\sqrt{2}T_0}\frac{A_g}{l_g a_g} \tag{5}$$

where γ is the ratio of specific heats of the air, P_0 (T_0) are the room pressure (temperature), and l_g is the layer of gas inside the chamber. Some frequency simulations of Eq. 5 are presented in Fig. 2 for some magnitude factors of α_s and k_s.

One can observe in Fig. 2 a faster decrease for signal amplitude when thermal parameters tend to smaller values. That agrees with the physical nature observed for diffusive thermal waves, where these two parameters (α_s and k_s) play an important role in the amount of heat reaching the gas chamber, contributing more, or less to the amplitude of photoacoustic signal.

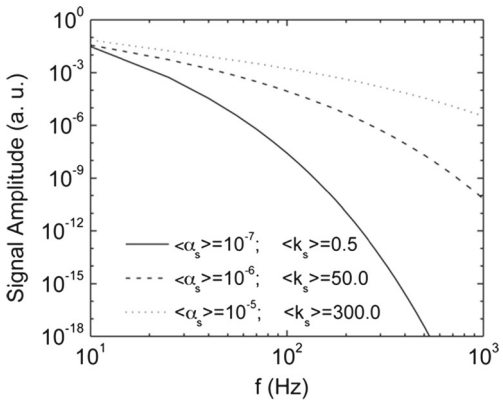

Fig. 2 A log-log graph for Eq. 5 versus f to three values of thermal diffusivity and conductivity, all divided (normalized) by its values at 10 Hz

2.2 Effect of the Metallic Layers to the Amplitude of the Photoacoustic Signal

When thickness of the sample is larger than thermal diffusion length ($l_s a_s >> 1$), the photoacoustic signal decreases exponentially with the root of the optical modulation frequency, ($\langle P\rangle \propto e^{-b\sqrt{f}}$), with $b = (\pi {l_s}^2/\alpha_s)^{1/2}$ [21, 22]. At this point, Eq. 5 can be written in the following expression:

$$\langle P\rangle = S_0\xi(f)\frac{e^{-l_s\sigma_s}}{\sigma_s a_g} \tag{6}$$

being $S_0 = \frac{\gamma P_0}{\sqrt{2}T_0 l_g}$ and $\xi(f) = \frac{4\epsilon_s\lambda_1 l_1 e^{l_2\sigma_g}}{e^{-2l_s\sigma_s}-1}$. In Eq. 6, $\xi(f)$ is slightly sensitive to thermal parameters of layers 1 and 2, but for thermally thick samples $\epsilon_2 \approx 0$ and $e^{l_1\sigma_1} = e^{l_2\sigma_2} \approx 1+l_1\sigma_1$, what contributes to its small variation in a wide range of frequency. So, an exponential decrease could be used in deriving effective thermal diffusivity for powder layer. Figure 3 shows the low influence of $\xi(f)$ over the signal when compared with Eq. 6 (for $<\alpha_s>= 10^{-7}$ m^2 s^{-1} and $<k_s> = 0.5$ W(mK)$^{-1}$).

3 Sample Preparation

Hydroxyapatite was obtained by calcination of bones taken from *armal* fish (*Pterodoras granulosus*), which live in Brazilian rivers, mainly in Mato Grosso, Mato Grosso do Sul, and Paraná states. The calcination process was made in a muffle furnace at 1173 K for 8 h in air atmosphere. That procedure was adopted as conditions are favorable for obtaining nanoparticles [11]. Some pieces of HAp were macerated manually before milling process on a high-energy mill (Retsch PM 100) at 300 rpm with a ball/weight ratio equals to 6/1 for 8 h. HAp particles have sizes between 200 and 1 μm.

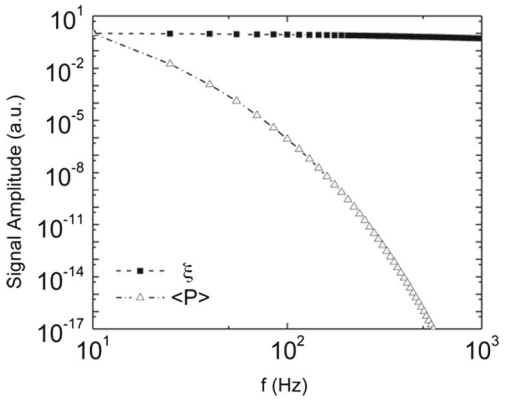

Fig. 3 A log-log graph comparing $\xi(f)$ and Eq. 6, both divided (normalized) by its values at 10 Hz

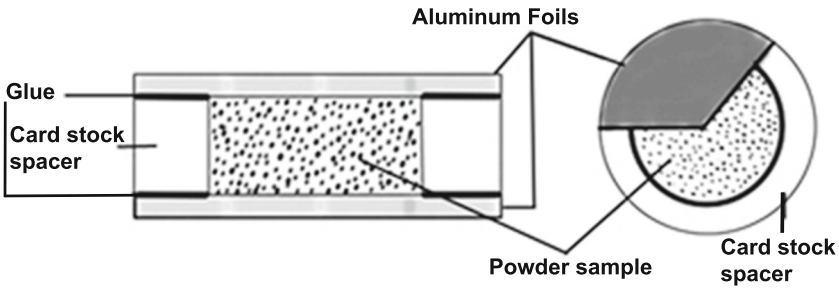

Fig. 4 Schematic diagram of the developed sample-holder for powder materials

Niobium pentoxide Nb_2O_5 was donated by a Brazilian Company of Metallurgy and Mining (CBMM) [9] in powder form (purity = 99.5 wt%). Nb_2O_5 grains were manually milled and then sieved to select sizes between 37 and 63 μm (larger than HAp particles). Each mixture was made according relation (1-x)(Hp)+(x)(Nb_2O_5) employed in powder metallurgy, where $0.0 \leq x \leq 1.0$.

Aluminum foils of 30 μm were used as layers for thermal coupling due to ease in its handling and obtention. In that case, the cut off frequency is little more than 30 kHz, ensuring a thermal diffusion length greater than thickness of metallic foils. Thus, for measurements up to 50 Hz, aluminum layers are thermally thin, with a minimum thermal diffusion length of about 771 μm. Figure 4 shows each constituent of sample-holder for storing the powder materials. Acrylic glue was used to seal each sample-holder. A total of 22 samples were prepared, being 2 samples to each code listed on Table 1.

3.1 Experiment

Figure 5 shows the schematic diagram for the photoacoustic apparatus. The heat source was a beam of 532 nm and 200 mW provided by a TTL laser. The beam modulation and microphone signal was generated and synchronized respectively by a lock-in amplifier (Stanford Research Systems SRS 830). The photoacoustic signal was detected with a high-sensitivity microphone (Sennheiser KE4-211-2) coupled to a linear pre-amplifier and filtered by the lock-in. The temperature was controlled at 298 K for all samples by a thermoelectric device (Wavelength Electronics controller LFI-3751). Such experimental setup could be applied on determination for thermal diffusivity as a function of temperature. One could investigate phase transitions for some materials as superconductors, magnetic ones, foods, drugs, and biological materials (like blood).

X-ray measurements were done in 2θ mode and steps of 2°/min, from 10 to 80° using radiation K_α from a copper anode (Shimadzu XRD-700). Micrographs were obtained at different magnifications by a scanning electron microscope (Shimadzu Superscan SS-550). Each sample was dispersed in acetone and placed on a metallic base, then were coated with a gold film by sputtering. The beam's energy of electrons was 15 keV.

Table 1 Codifications and properties for the samples related to the formula [(1-x)(HAp)+(x)(Nb_2O_5)]

Mixture codes	x value (%)	Thickness $l_s \pm 1$(μm)	Thermal diffusivity $\alpha_s(10^{-6}\ m^2\ s^{-1})$
HAp	0	302	7.7 ± 0.3
HAp9N1	10	291	6.5 ± 0.3
HAp8N2	20	303	9.8 ± 0.4
HAp7N3	30	321	8.1 ± 0.4
HAp6N4	40	315	9.6 ± 0.4
HAp5N5	50	309	7.7 ± 0.6
HAp4N6	60	307	7.5 ± 0.5
HAp3N7	70	311	6.4 ± 0.3
HAp2N8	80	305	4.8 ± 0.2
HAp1N9	90	295	2.9 ± 0.1
Nb_2O_5	100	298	0.70 ± 0.03

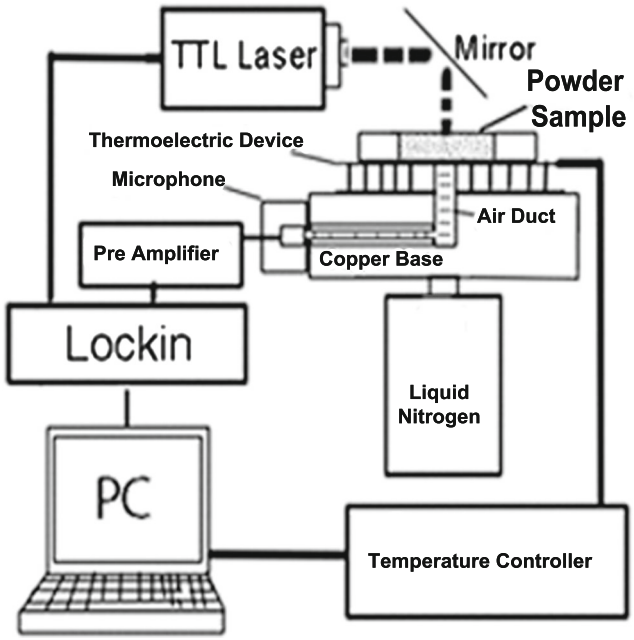

Fig. 5 Schematic diagram of the assembled photoacoustic apparatus

4 Results and Discussion

Figure 6 shows XRD results. The intensity variation for values of $x < 0.7$ (bellow HAp3N7) was less accentuated for peaks close to 40, 47, and 49°. These peaks were used as indicators for concentrations of each element on the mixture.

Figure 7 shows the frequency scans for the biocomposites (each curve is the mean obtained to two samples prepared for each code listed on Table 1). In comparison with thermally-thin and thermoelastic limits (curves $f^{-1.5}$ and f^{-1}, respectively) in Fig. 7a, it can be concluded that all samples are on the thermally thick regime for frequencies above 35 Hz. The thermoelastic effect, in this frequency range, has not been observed, mainly because the excitation beam was expanded to minimize the radial temperature gradient at the sample. Due to high scattering of the heat inside the powder, the occurrence of a temperature gradient and consequently the drum effect were frustrated. To determine the thermal diffusivity, it was used the parameter $b = (\pi . {l_s}^2/\alpha_s)^{1/2}$, adjusted from the curves presented in Fig. 7b. The error bars were obtained from propagation of error for parameters b and thickness l_s of the samples, and computed by Eq. 7

$$\delta\alpha = \pm 2\pi \left(\frac{l_s}{b}\right)^2 \cdot \left[\frac{\delta l_s}{l_s} + \frac{\delta b}{b}\right]. \quad (7)$$

The results for effective thermal diffusivity is shown in Fig. 8 as a function x. The measured values were between $(6.4 \pm 0.3) \times 10^{-6}$ m^2 s^{-1} and $(9.8 \pm 0.4) \times 10^{-6}$ m^2 s^{-1} for $x \leq 0.7$. For $x > 0.7$, the values decrease quickly to $(0.70 \pm 0.03) \times 10^{-6}$ m^2 s^{-1}. Table 1 lists the results obtained with photoacoustic method to all samples.The micrographs are presented in Fig. 9 (all with scales of 5 μm). A coat structure was observed for concentrations of $x \leq 0.7$, where small HAp particles adhere onto the Nb_2O_5.

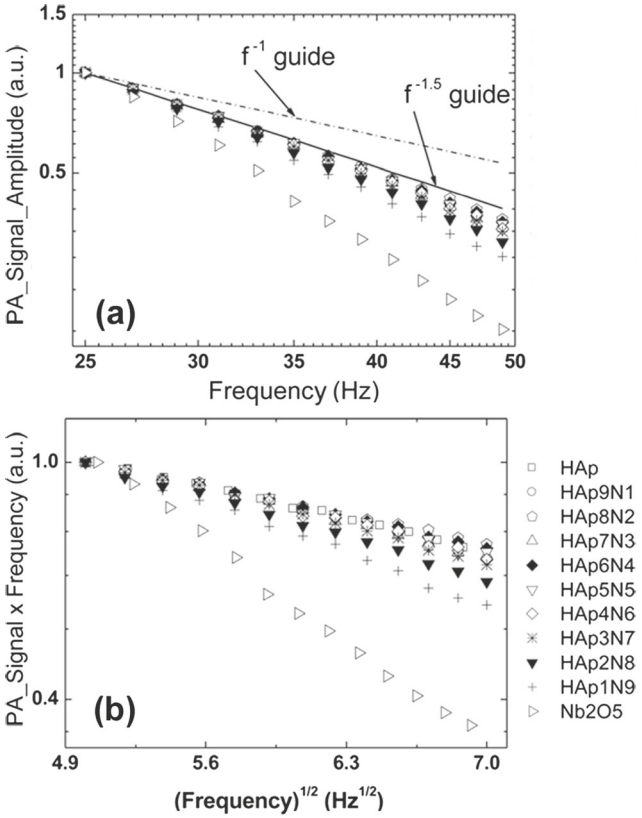

Fig. 7 **a** Experimental curves (in log-log scale) of photoacoustic rear signal amplitude as a function of optical modulation frequency compared with thermally-thin ($f^{-1.5}$ guide) and thermoelastic (f^{-1} guide) regimes. **b** Curves of frequency times photoacoustic signal amplitude (in a mono-logarithmic scale) versus the square root of the frequency

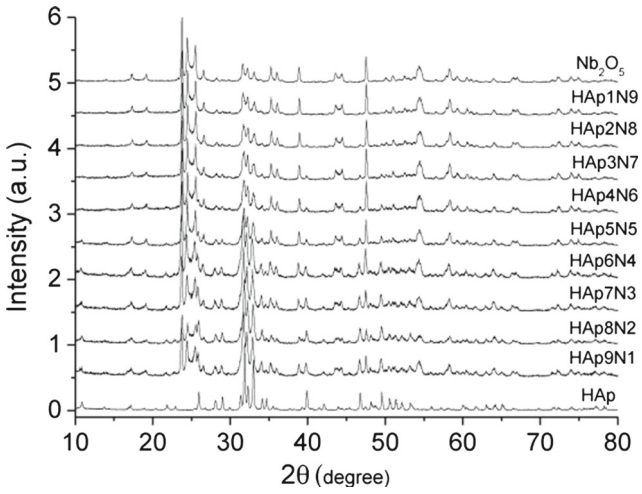

Fig. 6 X-ray diffractograms for each sample serving as references for concentrations of HAp and Nb_2O_5

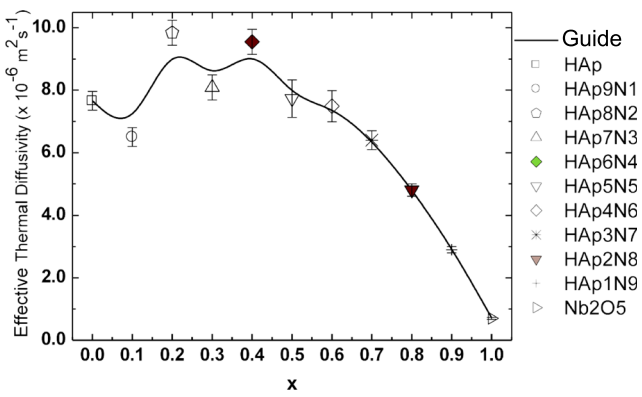

Fig. 8 Effective thermal diffusivity as a function of $x = Nb_2O_5$ concentration on HAp

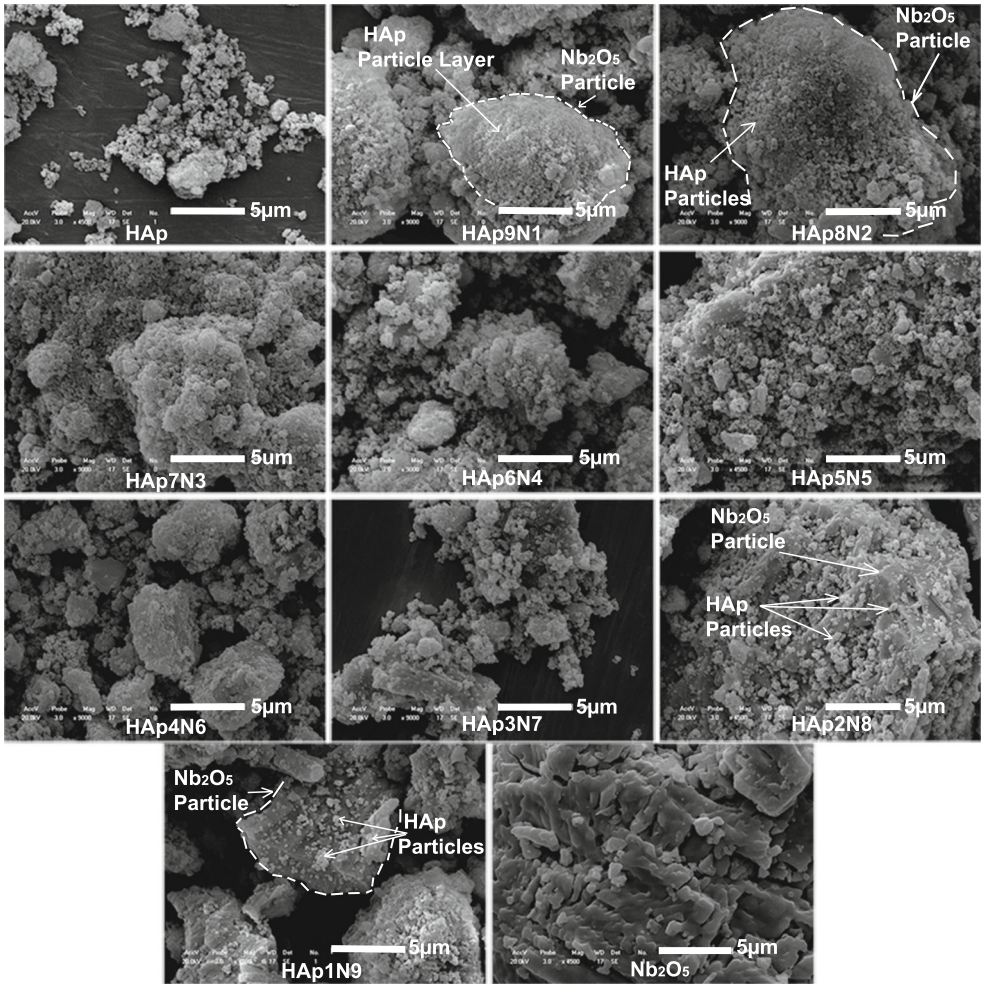

Fig. 9 Scanning electron microscopy (SEM) for mixtures (coded according Table 1)

5 Conclusion

An alternative way for thermally characterize powder materials based on detection of the rear photoacoustic signal is being presented. This technique was specifically applied in the study of biocompatible composites of hydroxyapatite HAp and niobium pentoxide Nb_2O_5. The effective thermal diffusivity was studied as a function of the Nb_2O_5 concentration mixed with the HAp. Experimental results for effective thermal diffusivity ranged from $(6.4 \pm 0.3) \times 10^{-6}$ m^2 s^{-1} to $(9.8 \pm 0.4) \times 10^{-6}$ m^2 s^{-1} for percentages of niobium pentoxide up to 70 %, and have decreased to values around $(0.70 \pm 0.03) \times 10^{-6}$ m^2 s^{-1} for concentrations of niobium pentoxide above 70 %. Results of scanning electron microscopy have shown a coat formed by small particles of HAp over Nb_2O_5 for some mixtures.

Acknowledgments The authors wish to thank the financial support given by the Brazilian agencies CNPq, CAPES, and Fundação Araucária-Paraná. In particular, we thank CBMM in collaboration with the engineer Rogério Ribas for having provided us with the Niobium pentoxide Nb_2O_5.

References

1. R. Gadow, A. Killinger, N. Stiegler, Hydroxyapatite coatings for biomedical applications deposited by different thermal spray techniques. Surf. Coat. Technol. **205**, 1157–1164 (2010)
2. A.C. Bento, D.P. Almond, S.R. Brown, I.G. Turner, Thermal and optical characterization of the calcium phosphate biomaterial hydroxyapatite. J. Appl. Phys. **79**, 6848 (1996)
3. R. Brayner, F. Bozon-Verduraz, Niobium pentoxide prepared by soft chemical routes; morphology, structure, defects and quantum size effect. Phys. Chem. Chem. Phys. **5**, 1457–1466 (2003)
4. S.V. Dorozhkin, Calcium orthophosphate-based biocomposites and hybrid biomaterials. J. Mater. Sci. **44**, 2343–2387 (2009)
5. R.L. Oréfice, M.M. Pereira, H.S. Mansur, *Biomateriais: Fundamentos e Aplicações* (Cultura médica, 2006)
6. J.B. Park, R.S. Lakes, *Biomaterials an Introduction* (Springer Science+Business Media, 2007)
7. C. Wanpeng, L.L. Hench, Bioactive materials. Ceram. Int. **22**, 493–507 (1996)
8. W.J. Nascimento, Preparação e Caracterização Físico-Mecânica, Microestrutural e Térmica de Compósitos à Base de Nióbio e Hidroxiapatita, Dissertação de Mestrado em Física, Universidade Estadual de Maringá (2009)
9. Companhia Brasileira de Metalurgia e Mineração (CBMM), September 2014. http://www.cbmm.com

10. W.R. Weinand, F.F.R. Gonçalves, W.M. Lima, Effect of sintering temperature in physical-mechanical behaviour and in titanium-hydroxyapatite composite sinterability, Mater. Sci. Forum, 249–254 (2006)
11. T.M. Coelho, E.S. Nogueira, A.S. Steimacher, A.N. Medina, W.R. Weinand, W.M. Lima, M.L. Baesso, A.C. Bento, Characterization of natural nanostructured hydroxyapatite obtained from the bones of Brazilian river fish. J. Appl. Phys. **100**, 094312 (2006)
12. W.J. Nascimento, T.G.M. Bonadio, V.F. Freitas, W.R. Weinand, M.L. Baesso, W.M. Lima, Nanostructured Nb_2O_5-natural hydroxyapatite formed by the mechanical aloyng method: a bulk composite. Mater. Chem. Phys. **130**, 84–89 (2011)
13. M. Kaviany, *Principles of Heat Transfer in Porous Media, Mechanical Engineering Series*, 2nd edn (Springer, New York, 1995)
14. C. Argento, D. Bouvard, Modeling the effective thermal conductivity of random packing of spheres through densification. Int. J. Heat Mass Transf. **39**, 1343–1350 (1996)
15. C. Argento, D. Bouvard, A ray tracing method for evaluating the radiative heat transfer in porous media. Int. J. Heat Mass Transf. **39**, 3175–3180 (1996)
16. J.A. Balderas-López, A. Mandelis, Novel transmission open photoacoustic cell configuration for thermal diffusivity measurements in liquids. Int. J. Theor. Phys. **23**, 605–614 (2002)
17. J.A. Mandelis, A. Balderas-López, J.A. García, Normalized photoacoustic techniques for thermal diffusivity measurements of buried layers in multilayered systems. J. Appl. Phys. **92**, 3047–3055 (2002)
18. D.P. Almond, P.M. Patel, *Photothermal Science and Techniques, Series in Physics and its Applications,* vol. 10 (Chapman & Hall, London, 1996)
19. A. Rosencwaig, A. Gersho, Theory of the photoacoustic effect with solids. J. Appl. Phys. **47**, 64–69 (1976)
20. A. Rosencwaig, *Photoacoustics and Photoacoustic Spectroscopy, Series of Monographs on Analytical Chemistry and its Applications* (Wiley, New York, 1980)
21. M.D. da Silva, I.N. Bandeira, L.C.M. Miranda, Open-cell photoacoustic radiation detector. J. Phys. E **20**, 1476–1478 (1987)
22. L.F. Perondi, L.C.M. Miranda, Minimalvolume photoacoustic cell measurement of thermal difussivity: effect of the thermoelastic sample bending. J. Appl. Phys. **62**, 2955–2959 (1987)